

# Self-supervised Learning of Pixel-wise Anatomical Embeddings in Radiological Images

Ke Yan<sup>1</sup>, Jinzheng Cai<sup>1</sup>, Dakai Jin<sup>1</sup>, Shun Miao<sup>1</sup>, Adam P. Harrison<sup>1</sup>, Dazhou Guo<sup>1</sup>, Youbao Tang<sup>1</sup>  
Jing Xiao<sup>2</sup>, Jingjing Lu<sup>3</sup>, and Le Lu<sup>1</sup>

<sup>1</sup> PAII Inc., 6720B Rockledge Drive, Suite 410, Bethesda, MD 20817

<sup>2</sup> Ping An Insurance (Group) Company of China, Ltd., Shenzhen, 510852, PRC

<sup>3</sup> Beijing United Family Hospital, Beijing, 100015, PRC

yankethu@gmail.com; tiger.lelu@gmail.com

## Abstract

*Radiological images such as computed tomography (CT) and X-rays render anatomy with intrinsic structures. Being able to reliably locate the same anatomical or semantic structure across varying images is a fundamental task in medical image analysis. In principle it is possible to use landmark detection or semantic segmentation for this task, but to work well these require large numbers of labeled data for each anatomical structure and sub-structure of interest. A more universal approach would discover the intrinsic structure from unlabeled images. We introduce such an approach, called Self-supervised Anatomical embedding (SAM). SAM generates semantic embeddings for each image pixel that describes its anatomical location or body part. To produce such embeddings, we propose a pixel-level contrastive learning framework. A coarse-to-fine strategy ensures both global and local anatomical information are encoded. Negative sample selection strategies are designed to enhance the discriminability among different body parts. Using SAM, one can label any point of interest on a template image, and then locate the same body part in other images by simple nearest neighbor searching. We demonstrate the effectiveness of SAM in multiple tasks with 2D and 3D image modalities. On a chest CT dataset with 19 landmarks, SAM outperforms widely-used registration algorithms while being 200 times faster. On two X-ray datasets, SAM, with only one labeled template image, outperforms supervised methods trained on 50 labeled images. We also apply SAM on whole-body follow-up lesion matching in CT and obtain an accuracy of 91%.*

## 1. Introduction

A fundamental task in medical image analysis is locating the same anatomical or semantic structure across different images. This can be addressed by organ segmen-

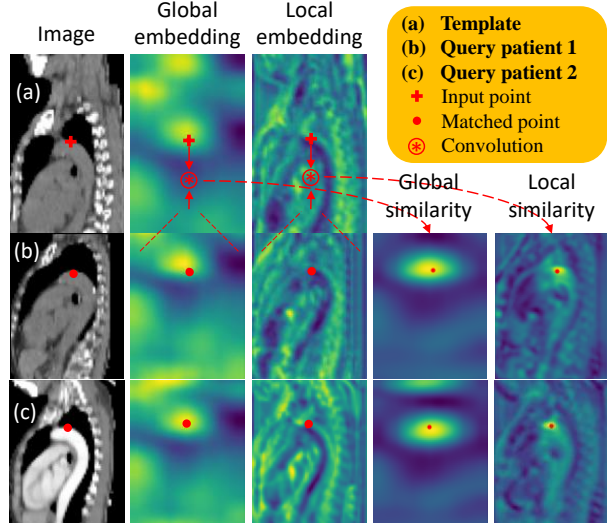


Figure 1: Anatomical location (top of aortic arch) matching results of self-supervised anatomical embedding (SAM).

tation [48, 16] or anatomical landmark detection [55, 23] algorithms. However, most supervised algorithms need sufficient labeled data for training. Annotating medical images is laborious, expensive, and requires considerable expertise [44]. Moreover, supervised models are restricted to only discovering organs or landmarks that were *a priori* labelled, but many labeled datasets are limited in their fine-grainedness. We notice that human organs are intrinsically structured, so there is an inherent consistency underlying their appearance and layout in radiological images such as computed tomography (CT) and X-rays. Intuitively, we can design an algorithm to discover these intrinsic patterns by learning from *unlabeled* images. Given a certain anatomical location (*e.g.*, top of aortic arch) in one image, the trained algorithm should be able to find the corresponding location in other images (see Fig. 1), although it was not trained specifically to detect the landmarks. We aim to develop

a universal algorithm that learns from unlabeled radiological images to detect arbitrary points of interest. It should generate an embedding on each image pixel to encode its anatomical context information, so that the same body part in different images express similar embeddings and can be retrieved by simple nearest neighbor searching. In this paper, we use the terms anatomical location or body part to describe the semantic location of a pixel, such as “center of the right lobe of thyroid” or “femur head”.

Learning anatomical embeddings that are universal across body parts, without anatomical labels in training, is a challenging task. For example, in CT images the algorithm has to memorize the 3D contextual appearance of numerous body parts so as to generate globally distinguishable embeddings. Meanwhile, it needs to encode local information to differentiate adjacent structures with similar appearance for accurate localization. In addition, the embeddings should be robust to the size, shape, intensity, and texture diversity of body parts, which may be caused by inter-subject variation, organ deformation, contrast injection, and pathological changes.

In this work, we propose Self-supervised Anatomical eMbedding (SAM) to achieve these goals. We adopt the recent self-supervised contrastive learning [49, 10, 17] approach and propose a pixel-level contrastive learning framework to differentiate pixels of varying body parts. During training, we use data augmentation to create synthetic body part pairs and simulate appearance changes across different images. To cover both global and local information, we design a coarse-to-fine architecture with two-level embeddings. The global embedding is trained to distinguish every body part on a coarse scale, helping the local embedding to focus on a smaller region to differentiate with finer features. The selection of negative samples (in our case, dissimilar body parts) is a crucial step of contrastive learning. We design several strategies to carefully control the difficulty and diversity of the selected negative samples. Finally, during inference, embeddings can be matched efficiently using 2D or 3D convolutional operations.

Due to its unsupervised and universal nature, SAM can be trained easily and applied to various tasks. First, a natural application is “one-shot” landmark detection with one labeled template image. We conduct such experiments on a chest CT dataset and two X-ray datasets (pelvis and hand) [23]. On the chest CT dataset, SAM outperforms widely-used deformable registration algorithms [2, 19, 39] while being  $>200$  times faster. On the X-ray datasets, our method with one labeled template outperforms the supervised HRNet [42] trained on 50 labeled images and a state-of-the-art graph convolutional network-based method [23] trained on five labeled images. Another application is lesion matching [54, 36], which is an important clinical task for radiologists to longitudinally track disease progress. On 1,014

lesion pairs manually annotated in the DeepLesion [53, 54] dataset, SAM outperforms previous supervised embedding-based algorithms [54, 52] (91% versus 82% in accuracy). While these results across diverse datasets are encouraging, we emphasize that this is a small sampling of the potential uses of the SAM embeddings.

Our major contributions are three-fold: **1)** The problem of universal anatomical embedding learning is tackled for the first time. We demonstrate that discriminative and robust embeddings can be learned in a self-supervised manner. **2)** A pixel-level contrastive learning framework is proposed with a coarse-to-fine architecture and customized negative sampling strategies. The proposed algorithm is easy to train and fast. **3)** The learned embeddings are used in various applications (landmark detection, lesion matching) on different image modalities (3D CT and 2D X-ray) of varying body parts (chest, hand, pelvis, etc.). Similar or superior performance is achieved compared to conventional registration or supervised algorithms.

## 2. Related Work

**Self-supervised learning (SSL).** In SSL, visual features are learned from unlabeled data by optimizing a heuristic pretext task, such as predicting image rotations [15] and inpainting [33]. Contrastive learning [49, 10, 17] uses image instance discrimination as the pretext task and has achieved promising performance. Recently, some SSL methods were developed to learn dense representations for semantic matching [30], object part segmentation [20], or network pretraining [35]. A latest method in [35] is closely related to ours as they also match corresponding pixels between images after data augmentation. However, [35] focused on network pretraining and was initialized from [17]. Our goal is not to pretrain networks, but to learn semantic anatomical embeddings that can be directly used in downstream tasks without finetuning. To achieve this goal, we designed novel coarse-to-fine architecture and sample selection strategies.

Radiological images are suitable for SSL because of the intrinsic structure of the human anatomy. The related work can be classified into three major categories. Content restoration algorithms [56, 13, 9] reconstruct original images from corrupted or cropped ones, aiming to pretrain network weights. Transformation prediction algorithms first do data augmentation to the image, and then predict the augmentation parameters, such as translation [4], patch order [57], and rotation [43]. Patch-wise [7] and superpixel-wise [32] contrastive learning have also been proposed to pretrain networks or learn representations for few-shot image segmentation. In contrast, we aim to learn pixel-wise representations to detect or match arbitrary anatomical points. While [7, 32] requires multi-stage training or superpixel extraction, our method is end-to-end trainable.

**Anatomy-related learning.** Anatomical landmark de-

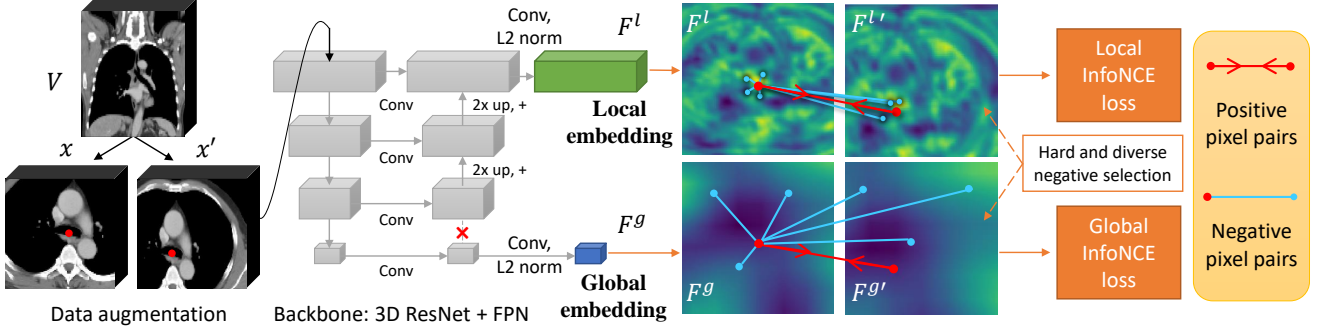


Figure 2: The learning process of SAM. We first do random data augmentation to an unlabeled image, then send the two transformed patches to a network to generate a global and a local embedding vector for each pixel. One embedding channel of an axial image slice is visualized in the figure with the global embedding zoomed in. Next, we use a global and a local InfoNCE loss [45] to encourage matched pixels (positive pairs) to have similar embeddings, while push unmatched ones (negative samples) apart. We designed strategies to select hard and diverse negatives for both global and local embeddings.

tection is important to initialize or aid many medical imaging tasks [23, 31, 8]. Heatmap [31] and coordinate-based [23] methods have been explored. Deep adaptive graphs were adopted in [23] to capture relationships among landmarks and achieved state-of-the-art results in three X-ray datasets. However, these methods all need training labels and can only predict the predefined anatomical positions, whereas our method is unsupervised and uses embedding matching to find arbitrary landmarks of interests. Anatomy-specific classification [38] or regression [51] methods can predict predefined body part classes or scores of CT slices. Compared to their slice-wise coarse predictions, our pixel-wise embedding is more fine-grained.

**Image registration** is popularly used to find pixel-wise correspondences in medical images. Traditional algorithms [39, 19, 2] iteratively optimize a predefined objective function for an image pair, which is often accurate but time-consuming. Recent deep learning-based methods [3, 41] directly predict a deformation field by using the spatial transformer network [21] to align the image pair. The main difference between registration and SAM is that registration requires an image pair as input and aims at aligning each pixel via fundamental appearance-based similarity measures, whereas SAM needs only one image and focuses on *semantically* representing each pixel. Last, **dense image description and matching** [25, 37, 11] are classic topics in computer vision, but not designed for medical images.

### 3. Method

The objective of self-supervised anatomical embedding (SAM) is to encode the semantic anatomical information of each pixel, so that similar body parts in different images can have similar embeddings. Inspired by previous works on contrastive learning [49, 10, 17], we propose a pixel-level contrastive learning framework as shown in Fig. 2. Essen-

tially, we let the model compare every part of the image to discover distinctive patterns by itself. The proposed framework comprises the following steps: stochastic data augmentation for training patch generation, coarse-to-fine CNN for pixel-wise feature embedding, and positive & negative sample selection for contrastive loss computation. In this section, we elaborate our framework for 3D images such as CT. It is straightforward to adapt SAM to 2D images such as X-ray by changing the network from 3D to 2D.

### 3.1. Coarse-to-Fine Network Architecture

To learn universal anatomical embeddings, on the one hand, SAM needs to memorize the 3D contextual appearance of numerous body parts so as to generate globally distinguishable embeddings. On the other hand, it needs to encode local information to differentiate adjacent structures with similar appearance for accurate localization. To get the best of both worlds, we propose a coarse-to-fine structure that predicts a global embedding and a local one for each pixel. A lightweight 3D ResNet-18 [18] is adopted as backbone with a feature pyramid network (FPN) [24] to fuse multi-scale features. The ResNet-18 is initialized with ImageNet pretrained weights using the inflated 3D technique [6]. The 4D global embedding tensor  $F^g$  and the local one  $F^l$  are both generated from the FPN features using separate  $3 \times 3 \times 3$  convolutions and L2 normalization layers.  $F^g$  is from the coarsest FPN level with larger strides and more abstract features, while  $F^l$  is from the finest FPN level with smaller strides and detailed features. Specifically, we cut the connection between the coarsest FPN feature and its upper level to make  $F^g$  and  $F^l$  more independent, see Fig. 2. Examples of the learned  $F^g$  and  $F^l$  can be found in Figs. 2 and 1, where  $F^l$  contains more high-frequency details.

### 3.2. Sampling Strategies and Loss Function

In every training batch, we randomly sample  $b$  unlabeled CT volumes. On each volume  $V$ , we crop two 3D patches with random location and size and resize them to the same shape, namely  $x, x' \in \mathbb{R}^{d \times h \times w}$ . When the two patches overlap, we can find pixel pairs from them so that each pair corresponds to the same position (body part) in the original volume. Since whole-body CT images are typically large ( $512 \times 512$  with hundreds of slices), randomly cropped patches sometimes do not overlap. It is important to keep these non-overlapping patch pairs since they can teach the model to differentiate body parts with large distances (e.g., neck and pelvis). We also performed other intensity and spatial transforms [10] to the patches, which will be discussed in the experiments section.

Next, we select positive and negative samples from the image patches. Compared with image-level contrastive learning [49, 10, 17], the pixel-level framework has abundant samples (pixels) in each training batch, so all samples can be selected efficiently within each batch. When image patches  $x$  and  $x'$  overlap, we randomly sample  $n_{\text{pos}}$  pixels  $p_i \in x$  from the overlapping area, each with a corresponding pixel  $p'_i \in x'$  to build a positive pair. The sampling position should avoid blank areas outside the body in CT. The positive embeddings at  $p_i, p'_i$  are  $f_i, f'_i \in \mathbb{R}^c, 1 \leq i \leq n_{\text{pos}}$ . When  $x$  and  $x'$  do not overlap, we randomly sample  $n_{\text{pos}}$  pixels from each patch and consider each embedding as being similar to itself. For each positive pair  $(p_i, p'_i)$ , we also find  $n_{\text{neg}}$  pixels as negative samples. They are randomly sampled from  $x$  and  $x'$  as long as their distance from  $p_i$  and  $p'_i$  is larger than  $\delta$  ( $\delta = 3\text{mm}$  in this paper). If we denote the embeddings at the negative pixels of pair  $i$  as  $h_{ij} \in \mathbb{R}^c, 1 \leq j \leq n_{\text{neg}}$ , the InfoNCE loss [45, 17] for this patch pair  $(x, x')$  is defined as

$$L = - \sum_{i=1}^{n_{\text{pos}}} \log \frac{\exp(f_i \cdot f'_i / \tau)}{\exp(f_i \cdot f'_i / \tau) + \sum_{j=1}^{n_{\text{neg}}} \exp(f_i \cdot h_{ij} / \tau)}, \quad (1)$$

where  $\tau = 0.5$  is a temperature parameter and  $\cdot$  is the inner product operation. We call  $f_i$  anchor embeddings. When  $x$  and  $x'$  do not overlap, we replace  $f'_i$  with  $f_i$  in Eq. (1). Since we want (1) to be symmetric with  $f_i$  and  $f'_i$  [10], another loss term with swapped  $f_i$  and  $f'_i$  is also computed and added. Eq. (1) is applicable to both global and local embeddings.

In our framework, the global embedding  $F^g$  is responsible for differentiating all body parts on a coarse scale. To make it more discriminative, we perform online **hard** negative selection [30, 40] to train it. For each global anchor embedding  $f_i^g$ , we compute its cosine similarity map with the global embedding tensors  $F^g$  and  $F^{g'}$  to get similarity maps  $S_i^g, S_i^{g'}$ . Then, hard negatives  $h_{ij}^g$  are selected to be the  $n_{\text{neg}}$  embeddings (that do not belong to  $f_i^g$  or  $f_i^{g'}$ ) with

---

### Algorithm 1 Self-supervised anatomical embedding (SAM)

---

**Input:** Unlabeled images  $\{V\}$ ;  $b, n_{\text{pos}}, n_{\text{neg}}, n_{\text{rand}}^g, n_{\text{cand}}^l$ .  
**Output:** Trained network.

- 1: Randomly select  $b$  images from  $\{V\}$ .
- 2: **for** each image **do**
- 3:     Run random data augmentation to get a patch pair  $(x, x')$ .
- 4:     Compute global and local embedding tensors of the two patches,  $F^g, F^{g'}, F^l, F^{l'}$ .
- 5:     Sample positive pixel pairs  $(p_i, p'_i)$ , then extract positive embeddings pairs  $(f_i^g, f_i^{g'}), (f_i^l, f_i^{l'})$ ,  $1 \leq i \leq n_{\text{pos}}$ .
- 6:     **for** each positive pair  $i$  **do**
- 7:         Compute similarity maps  $S_i^g, S_i^{g'}, S_i^l, S_i^{l'}$ .
- 8:         Find global hard negatives  $h_{ij}^g, 1 \leq j \leq n_{\text{neg}}$ .
- 9:         Sample global random negatives  $h_{ik}^g, 1 \leq k \leq n_{\text{rand}}^g$  from all  $b$  patch pairs in the training batch. Pool the hard and random negatives to get the final global negatives.
- 10:         Find local hard negatives  $h_{ij}^l, 1 \leq j \leq n_{\text{cand}}^l$ . Randomly sample  $n_{\text{neg}}$  from them as the final local negatives.
- 11:     **end for**
- 12:     Compute the global and local InfoNCE loss  $L^g, L^l$  in Eq. (1). The final loss is  $L = L^g + L^l$ .
- 13: **end for**

---

the greatest similarity with  $f_i^g$ . To further aid training, we populate the negative samples to contain more **diverse** body parts. For each  $f_i^g$ , we randomly sample an additional  $n_{\text{rand}}^g$  pixels from all patches *across all volumes* within a training batch. Because these pixels originate from different image volumes it is very unlikely the sampled pixels are in the same semantic position as  $f_i^g$ .

Moving on to the local embedding, it uses the same positive pixel pairs  $(p_i, p'_i)$  as the global version, but with different negative samples. For each local anchor  $f_i^l$ , we first compute its local similarity maps  $S_i^l, S_i^{l'}$  with  $F^l, F^{l'}$ , then upsample  $S_i^g, S_i^{g'}$  to be the same size as  $S_i^l$ , and finally use the combined global and local similarity maps  $S_i^g + S_i^l, S_i^{g'} + S_i^{l'}$  to select **hard** negatives pixels for  $f_i^l$ . Examples of  $S^l$  and upsampled  $S^g$  can be found in Figs. 3 and 1. When the global embedding converges,  $S_i^g$  will be high only in the neighborhood area of  $p_i$  and  $p'_i$ , so that hard negatives can be selected mostly in the local area. During inference we use the peak of  $S^g + S^l$  to find matched points, so using  $S^g + S^l$  for local hard negative selection is consistent with our inference process. Meanwhile, because the local embedding tensor has a high resolution, the selected local hard negatives will mostly be adjacent pixels and correlated. To improve **diversity**, we first find the top  $n_{\text{cand}}^l > n_{\text{neg}}$  hard negative candidates, then randomly sample  $n_{\text{neg}}$  embeddings from them to be used in Eq. (1). The complete training procedure is summarized in Algorithm 1.

### 3.3. Inference

The inference procedure of SAM for anatomical location matching is illustrated in Fig. 3. To locate a certain point of

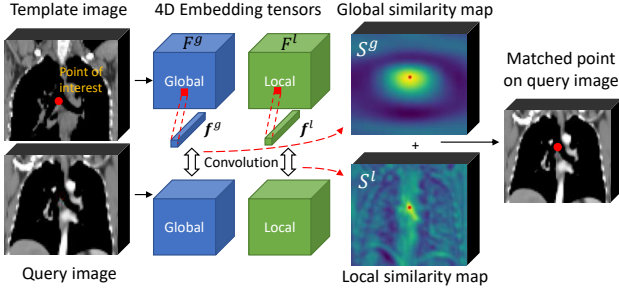


Figure 3: The inference procedure of SAM. Red dots on each image are the point of interest or matched point.

interest, we first need to label it on a template image (also known as an atlas [46] or support image [32]). Then, given an unlabeled query image, we compute the global and local embedding tensors, extract the anchor embedding vectors from the point of interest of the template, and compute the similarity maps  $S^g, S^l$  between the anchor and the query embedding tensors. Since the embeddings are L2-normalized, the cosine similarity maps can be efficiently computed using the convolutional operation on GPU. Finally, we upsample  $S^g, S^l$  to the size of the original image, and find the peak of  $S^g + S^l$  as the detected anatomical location.

## 4. Experiments

We evaluate SAM on four diverse tasks: 3D landmark detection on chest CT, 2D landmark detection on hand and pelvic X-rays, and 3D universal lesion matching on CT. Comprehensive ablation studies are performed to analyze the effect of the proposed coarse-to-fine structure and negative sampling strategies, as well as the selection of data augmentation approaches and other hyper-parameters. We also compare our self-supervised method with widely-used registration methods [19, 2, 39], supervised landmark detection [42, 23] and embedding learning [54, 52] methods.

### 4.1. Tasks and Datasets

For the two CT-based tasks, we trained a unified SAM model using the combination of three CT datasets: DeepLesion, NIH-Lymph Node (NIH-LN), and an in-house chest CT dataset (ChestCT). DeepLesion [53, 54] is a large CT dataset with 20K sub-volumes covering the whole body. It contains a variety of contrast phases, reconstruction protocols, and pathology. NIH-LN [1] includes 176 chest-abdomen-pelvis CT scans. ChestCT contains 94 patients, each with a contrast-enhanced (CE) and a non-contrast (NC) scan that are pre-aligned. When training SAM, no labels from the three datasets were used. We followed the official data split for DeepLesion, while used all images in NIH-LN for training. For ChestCT, we randomly split the patients to 65 training, 11 validation, and 18 testing.

**3D landmark detection** is tested using ChestCT, which contains manual annotations of 35 organs for each patient. We calculated 19 landmarks to evaluate SAM, such as the top of left lung, the bifurcation of trachea, etc. To detect landmarks in the one-shot setting, we need to select a template image from the training set. The sample whose landmarks are closest to the average normalized landmarks was chosen as the template [47]. More details about the template selection and landmarks are in the supplementary material.

**2D landmark detection** is conducted on X-rays following the settings in [23]. The hand and pelvic models were trained separately. The hand X-ray dataset contains 378 images for training and 93 for testing. Images were taken in different hand poses with resolutions in  $\sim 1500 \times 2000$ . 30 landmarks were manually labeled in each image. The pelvic X-rays were taken of each patient's pelvic bone with resolutions of  $\sim 2500 \times 2000$ . 800 images were used for training and 200 for testing. The template images were chosen in the same way as in ChestCT. In both hand and pelvic X-rays, there are high structural and appearance variations, caused by various pathologies (e.g., arthritis, bone fractures and metal prosthesis)

**3D Lesion matching** is tested using DeepLesion, which includes 32K lesions annotated on 4K patients. Most patients have multiple follow-up CTs. Given a lesion annotation on one CT, the task of lesion matching is to locate the corresponding lesion on another CT of the same patient. We manually annotated 1,014 lesion pairs on the validation and test sets of DeepLesion. A latest lesion detection algorithm [5] was used to generate the 3D bounding-box of each lesion. Then, we extracted the embedding from the center of the box of the template lesion, and use it to detect a matched point in the follow-up scan.

**Evaluation metrics:** We use the mean radial error (MRE) [23] and maximum radial error as the evaluation metrics. Radial errors are the Euclidean distances of predicted and ground-truth coordinates. For lesion matching, the central points of the lesions' 3D bounding-boxes are used as landmarks to compute errors. Besides, if the matched point falls in the lesion's bounding-box, it is regarded as a correct match to calculate the accuracy.

### 4.2. Implementation Details

SAM was implemented in PyTorch with the help of data augmentation libraries [12, 34]. It was trained using rectified Adam (RAdam) [27] with a learning rate of 0.0001. The batch size  $b$  was 8 for CT and 16 for X-ray. All models converged in about 25K iterations. We normalized CT images to a spacing of  $2 \times 2 \times 2 \text{ mm}^3$ , whereas the X-ray images were resized to  $512 \times 512$  as in [23]. The patch size was  $32 \times 96 \times 96$  for CT and  $400 \times 400$  for X-ray. The backbone network was 3D ResNet-18 for CT and 2D ResNet-34 for X-ray. Further increasing the net-

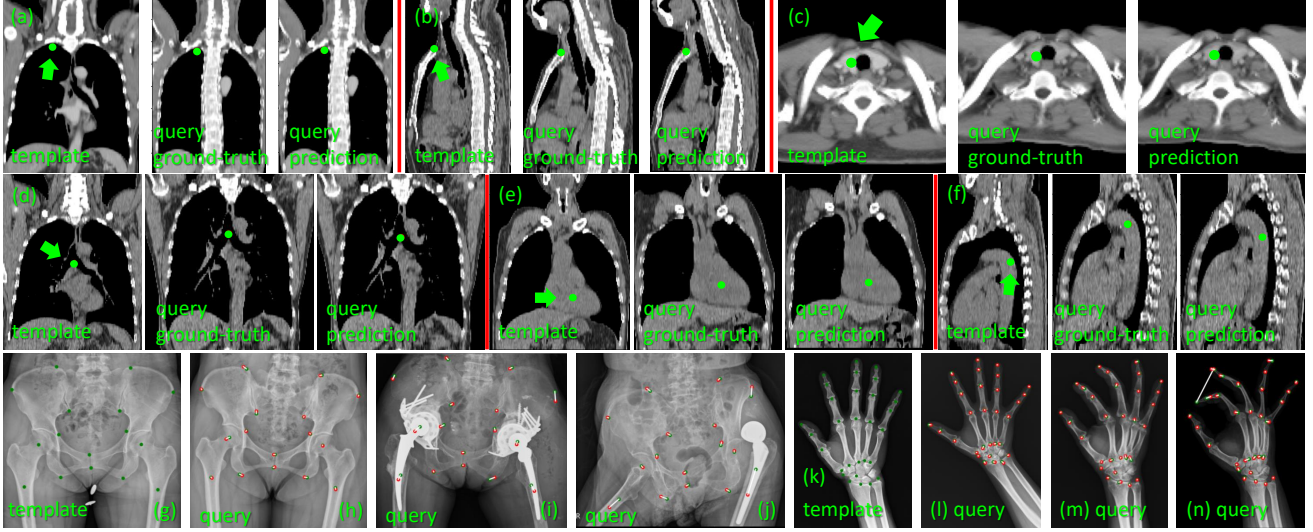


Figure 4: Examples of landmark detection results of SAM. Each image type (chest CT, pelvic X-ray, and hand X-ray) has only one template image. For CT images (a–f), the views (axial, coronal, sagittal) were selected in order to clearly show the point. For X-ray images (g–n), the green and red points are respectively ground-truth and predicted points, while the white lines show their correspondence. (f), (j), and (n) are failure cases in which the prediction errors are larger.

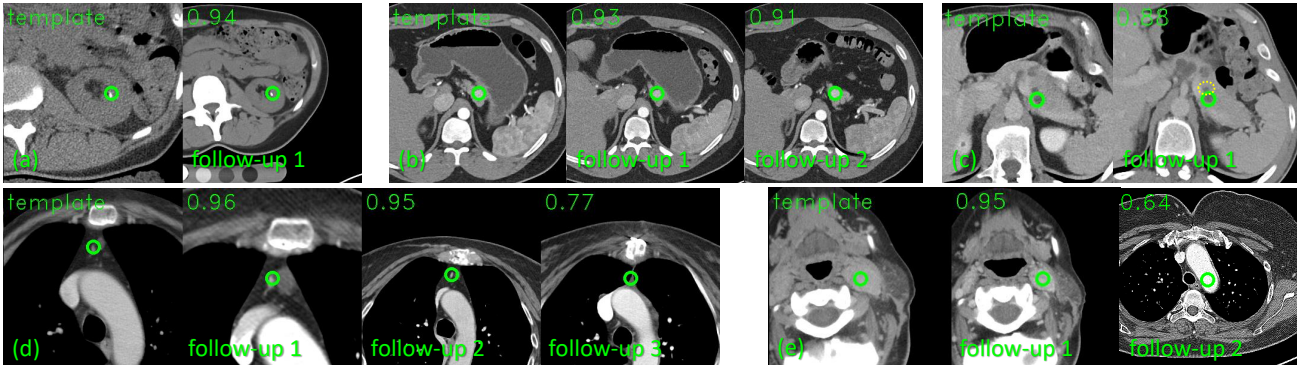


Figure 5: Examples of lesion matching results of SAM on DeepLesion. Green circles mark the lesion’s central point in the template scan and the detected points in follow-up scans. The predicted similarity scores are also shown. The dashed circle in (c) follow-up 1 is another adjacent lesion. Follow-up 2 of (e) is from a CT volume that does not include the neck region.

work depth did not result in significant improvements. To enlarge the resolution of the feature maps, we changed the strides in  $x, y$  axes to 1 in the conv1 block and the  $z$  stride to 1 in conv1, conv3, and conv4 [18]. The strides of the global and local embeddings for CT are  $4 \times 16 \times 16$  and  $2 \times 2 \times 2$ , respectively. For X-ray, they are  $16 \times 16$  and  $2 \times 2$ . The global and local embedding dimensions are both  $c = 128$ . The default sampling hyper-parameters for CT are  $n_{\text{pos}} = 100$ ,  $n_{\text{neg}} = 500$ ,  $n_{\text{rand}}^g = 1000$ , and  $n_{\text{cand}}^l = 2 \times 10^4$ . For X-ray, they are the same except for  $n_{\text{cand}}^l = 5000$  as we hope the local embedding to be more locally focused in 2D images. We will study the selection of the hyper-parameters and show that SAM is robust to their values.

### 4.3. Qualitative Results

As shown in Fig. 4, SAM is able to accurately detect various landmarks in different body parts with only one template image. In (e), it precisely locates the center of the heart in a texture-less non-contrast CT. In (f), the detection of the top of the descending aorta is off in the  $z$ -axis. This is because the appearance difference between the true and predicted points in the  $z$ -axis is not discriminative enough, while the image context in the  $x, y$ -plane has inter-subject variability for this landmark. For X-ray images, SAM can locate the landmarks in the presence of body rotation, deformation, and metal prostheses. Failure cases occur when there are severe pathological deformations that significantly

Method	ChestCT CE		ChestCT NC		Hand X-ray		Pelvic X-ray		Universal lesion matching		
	MRE	Max	MRE	Max	MRE	Max	MRE	Accuracy	MRE	Max	
(a) SAM (proposed)	<b>4.3±3.0</b>	<b>16.4</b>	<b>4.5±3.0</b>	<b>18.5</b>	<b>13.1±32.3</b>		<b>32.2±26.2</b>	91.1	<b>2.7±2.5</b>	<b>28.8</b>	
(b) w/o coarse-to-fine structure	4.9±3.0	17.4	5.2±4.3	61.2	26.1±70.0		34.4±31.6	84.1	3.5±3.1	41.1	
(c) Test: Global embedding only	9.9±12.1	80.1	9.4±10.4	79.3	437.0±431.1		48.8±28.8	52.5	6.6±3.2	29.9	
(d) Test: Local embedding only	6.3±12.2	150.1	6.5±9.2	84.7	473.4±519.2		34.6±43.3	90.1	3.2±6.6	130.4	
(e) w/o hard negative in global	<b>4.3±3.1</b>	20.8	<b>4.6±3.1</b>	20.8	17.9±55.0		32.7±25.8	90.7	2.7±2.6	31.6	
(f) w/o diverse negative in global	4.4±3.0	<b>16.4</b>	4.8±5.2	85.0	<b>14.4±38.2</b>		<b>32.0±25.2</b>	90.0	2.8±2.6	<b>28.8</b>	
(g) w/o hard negative in local	4.6±3.4	18.1	4.7±3.3	<b>18.7</b>	17.4±31.5		41.4±30.8	89.0	3.0±2.7	<b>27.9</b>	
(h) w/o diverse negative in local	4.7±5.8	94.0	5.3±7.0	94.2	16.6±47.2		43.7±40.5	<b>92.7</b>	<b>2.5±2.6</b>	28.8	
(i) SAM trained on NIH-LN alone	4.5±3.3	20.8	4.9±3.7	24.2	—	—	—	<b>91.4</b>	<b>2.7±2.6</b>	30.7	

Table 1: Ablation study of the proposed method. The top two best results in each metric are shown in bold. CE: contrast-enhanced; NC: non-contrast; MRE: mean radial error±std.; Max: maximum radial error. Errors are calculated in pixels.

differ from the template image.

SAM can match a variety of lesions effectively in follow-up CTs, see Fig. 5. In (a), it located a tiny lesion despite the image noise in the template. In (b), SAM detected the lesion in follow-up 2 although it has a different context than the template (notice the stomach). In (c), the algorithm successfully differentiated the true matched lesion from an adjacent one. (d) is an interesting case where the lesion disappeared in follow-up 3 possibly due to surgery. SAM can locate the correct position even if the lesion no longer exists, showing that it has learned the body part from the anatomical context. Besides, follow-up 1 in (d) is a CT scan with a limited field of view, which SAM handled well. Sometimes a lesion in the template scan may not exist in the follow-up scan due to the scanning range differences in  $z$ -axis, which is the case in follow-up 2 of (e). SAM detected an unrelated point with a low similarity score, which can be filtered with a score threshold when used in practice. More results will be shown in the supplementary material.

#### 4.4. Ablation and Parameter Study

**Coarse-to-fine embedding architecture:** Table 1 exhibits quantitative results of landmark detection and lesion matching on the four datasets. SAM’s accuracy is consistently high in all tasks. The coarse-to-fine embedding learning strategy is important to SAM. We tested to only learn one embedding for each pixel as in [35] by removing the global embedding. As shown in row (b), the results decreased considerably in all tasks, indicating that single-scale embeddings struggle to encode both global and local anatomical information. We also trained both global and local embeddings but only used one of them for inference, where the results were not promising as shown in rows (c) and (d). The global embedding can provide a rough localization but may not be very accurate (see the small offsets between the global similarity peaks and the red points in Figs. 1 and 3). The local one can locate more precisely but also highlight distant areas with similar local textures if the

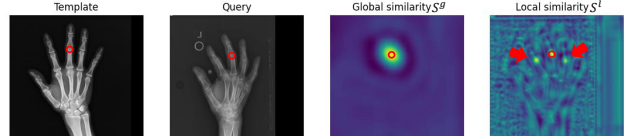


Figure 6: An example in the hand X-ray dataset. Red circles show the ground-truth landmarks. Arrows indicate spurious highlights in the local similarity map of the query image.

Method	ChestCT	ChestCT	Hand	Pelvic	Lesion
	CE	NC	X-ray	X-ray	match.
Crop only	4.7	4.7	26.7	32.6	2.8
+ Scaling	<b>4.3</b>	4.6	21.9	32.9	2.7
+ Intensity jitter	<b>4.3</b>	<b>4.5</b>	22.6	33.8	2.7
+ Def. & Rot.	4.5	4.6	<b>13.1</b>	<b>32.2</b>	<b>2.6</b>
+ Flip	4.6	5.0	64.9	326.4	2.8

Table 2: MRE with different data augmentation used in training. We start with random crop and add more augmentations step-by-step. Def. & Rot.: deformation and rotation.

global similarity is not considered, leading to a large maximum error. This can be further illustrated in Fig. 6.

**Sampling strategies:** Applying hard and diverse negative sampling generally improves performance. The diverse negative means the  $n_{\text{rand}}^g$  random negatives in global embeddings, and the  $n_{\text{neg}}$  random negatives sampled from  $n_{\text{cand}}^l$  hard ones in local embeddings. For example, in row (h), if we only sample hard negatives in local embedding learning, the maximum error will increase, possibly because the model overfit to the hard examples in the training set, so produced more distant false highlights in the test set. In row (i), we trained SAM on the NIH-LN dataset and tested on DeepLesion and ChestCT. Its performance degraded slightly compared to (a) which used DeepLesion and ChestCT in training, showing that the learned anatomical embeddings of SAM is generalizable across datasets.

**Data augmentation:** Table 2 analyzes the effect of dif-

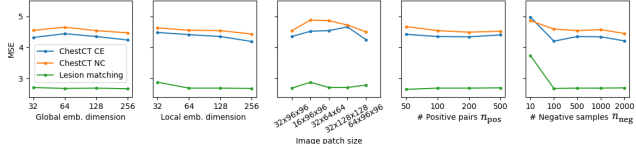


Figure 7: Parameter study on the ChestCT and lesion matching datasets. Please zoom in on a digital device.

	CE MRE	CE Max	NC MRE	NC Max	Time (s)
Affine [22]	8.4±5.2	32.9	8.5±5.3	33.1	6.82
FFD [39]	5.4±4.1	29.1	5.5±3.9	24.6	86.66
SyN [2]	5.1±3.7	21.9	5.3±3.7	22.9	78.58
DEEDS [19]	4.6±3.3	18.8	4.7±3.3	18.9	50.16
SAM	<b>4.3±3.0</b>	<b>16.4</b>	<b>4.5±3.0</b>	<b>18.5</b>	<b>0.23</b>

Table 3: Comparison of methods on the ChestCT dataset.

ferent data augmentation approaches, which is key to contrastive learning [10]. Results show that random cropping and scaling suffice to learn good embeddings in CT, while random deformation and rotation (within 30°) is crucial for hand X-ray, as rotated and deformed hands are common in the dataset. Random flipping harms performance as the medical images we used are normalized in their coordinate space. For pelvic X-rays, it is hard to distinguish their left and right sides, so flipped images confused model training. To sum up, a data augmentation approach for learning effective anatomical embedding is essential only if the corresponding image variance commonly exists in the data.

**Parameter study:** The influence of parameter values is investigated in Fig. 7. We can see that SAM is robust to embedding dimensions, although larger dimensions slightly improved performance [10]. The size of the image patch in  $z$ -axis should not be too small ( $\geq 32$  pixels). SAM is robust to  $n_{\text{pos}}$  and  $n_{\text{neg}}$  as long as  $n_{\text{neg}} \geq 100$ .

#### 4.5. Comparison to Previous Work

For the 3D landmark detection task, we compared with four widely used conventional registration methods [2, 19, 22, 39] in one-shot (single atlas) setting. The template CT image in the training set was registered respectively to the images in the test set. The landmark detection errors were shown in Table 3. Free-Form Deformation (FFD) [39] and Symmetric Normalization (SyN) [2] are the top-performing methods in registering chest CTs [29], while DEEDS [19] performed the best in a recent survey [50] and was shown to be more accurate than a recent deep learning-based approach [26]. SAM consistently outperformed these registration methods in all metrics using both contrast-enhanced (CE) and non-contrast (NC) CT, while only took 0.23s to process one volume. Deformable registration methods require a robust initial alignment to perform well, and may

Method	#Labeled samples	Pelvic X-ray	Hand X-ray
HR-Net [42]	5	139.1±327.5	43.3±112.0
	50	35.1±78.1	14.1±14.7
DAG [23]	5	35.3±53.2	16.4±39.5
	50	<b>21.5±19.84</b>	<b>6.2±4.2</b>
SAM	1	32.2±26.2	13.1±32.3

Table 4: Comparison of methods on the X-ray datasets.

struggle when the two images exhibit large differences in terms of body size/pose, organ shape and respiratory status [50]. In contrast, SAM is able to encode semantic and fine-grained anatomical information, which addressed the landmark matching problem effectively from another direction. We further used a CE template to detect landmarks in NC images, and vice versa. SAM’s MREs are 4.5 and 4.8 (DEEDS: 4.7, 4.7). They are comparable to the results using the same modality to train and test (4.5 and 4.3), showing SAM’s robustness to contrast changes in CT.

For the 2D X-ray landmark detection tasks, we compared with a strong supervised baseline HRNet [42] and a state-of-the-art method on X-rays, Deep Adaptive Graph (DAG) [23]. We retrained them in the few-shot setting. In Table 4, SAM outperformed HRNet trained on 50 samples, and DAG trained on 5 samples. It shows the efficacy of our method since it only used one labeled template. Methods to leverage more templates to improve accuracy will be our future work. Supervised methods are dedicated to modeling specific landmarks, thus may take advantage of the labeled samples better than self-supervised methods. However, they can only detect what has been *a priori* labelled, while SAM can detect arbitrary anatomical locations.

For the lesion matching task, we assessed two supervised lesion embedding methods trained on manual labels [54] or labels mined from radiological reports [52]. Since they need the bounding-box of the lesion as input, we used a lesion detector VULD [5] to first detect all lesion candidates in the query CT, and then matched them with the template lesion. The accuracies were 80.7% for lesion embedding [54] and 82.1% for LesaNet [52], both significantly lower than 91.1% for SAM. The bottleneck of these detection+matching methods is detection, since it is difficult to find all lesion candidates especially when they are small and subtle (Fig. 5(d)). The detection recall is only 87.3% in our experiment. Therefore, our direct matching strategy is more suitable by avoiding the intermediate detection step.

## 5. Conclusion

In this paper, we proposed self-supervised anatomical embedding (SAM) to learn pixel-wise anatomical representation from unlabeled radiological images. SAM can be used to locate arbitrary body parts with only one labeled

template. It is fast, robust to common image variations, and applicable to various image modalities and body parts. Experiments showed it outperformed registration algorithms and supervised methods in few-shot scenarios. Besides universal landmark detection and lesion matching, SAM can potentially be used to aid and improve other medical image analysis tasks such as registration [28], lesion detection [14], and retrieval [54], by providing fine-grained location cue and discriminative semantic features.

## References

- [1] CT Lymph Nodes dataset - The Cancer Imaging Archive (TCIA) Public Access, 2016. [5](#)
- [2] B B Avants, C L Epstein, M Grossman, and J C Gee. Symmetric diffeomorphic image registration with cross-correlation: Evaluating automated labeling of elderly and neurodegenerative brain. *Med. Image Anal.*, 12(1):26–41, 2008. [2, 3, 5, 8, 15](#)
- [3] Guha Balakrishnan, Amy Zhao, Mert R Sabuncu, John Guttag, and Adrian V Dalca. VoxelMorph: A Learning Framework for Deformable Medical Image Registration. *IEEE Trans. Med. Imaging*, 38(8):1788–1800, 2019. [3](#)
- [4] Maximilian Blendowski, Hannes Nickisch, and Mattias P Heinrich. How to Learn from Unlabeled Volume Data: Self-supervised 3D Context Feature Learning. In *MICCAI*, volume 11769 LNCS, pages 649–657, 2019. [2](#)
- [5] Jinzheng Cai, Ke Yan, Chi-Tung Cheng, Jing Xiao, Chien-Hung Liao, Le Lu, and Adam P Harrison. Deep Volumetric Universal Lesion Detection Using Light-Weight Pseudo 3D Convolution and Surface Point Regression. In *MICCAI*, pages 3–13, 2020. [5, 8](#)
- [6] João Carreira and Andrew Zisserman. Quo Vadis, action recognition? A new model and the kinetics dataset. In *Proc. IEEE Conf. Comput. Vis. Pattern Recognit.*, volume 2017-Janua, pages 4724–4733, 2017. [3](#)
- [7] Krishna Chaitanya, Ertunc Erdil, Neerav Karani, and Ender Konukoglu. Contrastive learning of global and local features for medical image segmentation with limited annotations. In *NeurIPS*, 2020. [2](#)
- [8] Haomin Chen, Yirui Wang, Kang Zheng, Weijian Li, Chi-Tung Cheng, Adam P Harrison, Jing Xiao, Gregory D Hager, Le Lu, Chien-Hung Liao, and Shun Miao. Anatomy-Aware Siamese Network: Exploiting Semantic Asymmetry for Accurate Pelvic Fracture Detection in X-ray Images. In *ECCV*, 2020. [3](#)
- [9] Liang Chen, Paul Bentley, Kensaku Mori, Kazunari Misawa, Michitaka Fujiwara, and Daniel Rueckert. Self-supervised learning for medical image analysis using image context restoration. *Med. Image Anal.*, 58:101539, 2019. [2](#)
- [10] Ting Chen, Simon Kornblith, Mohammad Norouzi, and Geoffrey Hinton. A Simple Framework for Contrastive Learning of Visual Representations. In *ICML*, 2020. [2, 3, 4, 8](#)
- [11] Mihai Dusmanu, Ignacio Rocco, Tomas Pajdla, Marc Pollefeys, Josef Sivic, Akihiko Torii, and Torsten Sattler. D2-net: A trainable CNN for joint description and detection of local features. In *CVPR*, volume 2019-June, pages 8084–8093, 2019. [3](#)
- [12] Isensee Fabian, Jäger Paul, and Wasserthal Jakob. batchgenerators - a python framework for data augmentation. Technical report, 2020. [5](#)
- [13] Ruibin Feng, Zongwei Zhou, Michael B Gotway, and Jianming Liang. Parts2Whole: Self-supervised Contrastive Learning via Reconstruction. In *MICCAI Work. Domain Adapt. Represent. Transf.*, 2020. [2](#)
- [14] Mohsen Ghafoorian, Nico Karssemeijer, Tom Heskes, Mayra Bergkamp, Joost Wissink, Jiri Obels, Karlijn Keizer, Frank Erik de Leeuw, Bram van Ginneken, Elena Marchiori, and Bram Platel. Deep multi-scale location-aware 3D convolutional neural networks for automated detection of lacunes of presumed vascular origin. *NeuroImage: Clinical*, 14:391–399, jan 2017. [9](#)
- [15] Spyros Gidaris, Praveer Singh, and Nikos Komodakis. Unsupervised representation learning by predicting image rotations. In *ICLR*, 2018. [2](#)
- [16] Dazhou Guo, Dakai Jin, Zhuotun Zhu, Tsung-Ying Ho, Adam P. Harrison, Chun-Hung Chao, Jing Xiao, and Le Lu. Organ at Risk Segmentation for Head and Neck Cancer Using Stratified Learning and Neural Architecture Search. In *CVPR*, pages 4222–4231, 2020. [1](#)
- [17] Kaiming He, Haoqi Fan, Yuxin Wu, Saining Xie, and Ross Girshick. Momentum Contrast for Unsupervised Visual Representation Learning. In *CVPR*, pages 9726–9735, 2020. [2, 3, 4](#)
- [18] Kaiming He, Xiangyu Zhang, Shaoqing Ren, and Jian Sun. Deep Residual Learning for Image Recognition. In *CVPR*, pages 770–778, 2016. [3, 6, 16](#)
- [19] Mattias P Heinrich, Mark Jenkinson, Michael Brady, and Julia A Schnabel. Mrf-based deformable registration and ventilation estimation of lung ct. *IEEE transactions on medical imaging*, 32(7):1239–1248, 2013. [2, 3, 5, 8, 15](#)
- [20] Wei Chih Hung, Varun Jampani, Sifei Liu, Pavlo Molchanov, Ming Hsuan Yang, and Jan Kautz. SCOPS: Self-supervised co-part segmentation. In *CVPR*, 2019. [2](#)
- [21] Max Jaderberg, Karen Simonyan, Andrew Zisserman, et al. Spatial transformer networks. In *Advances in neural information processing systems*, pages 2017–2025, 2015. [3](#)
- [22] Stefan Klein, Marius Staring, Keelin Murphy, Max A. Viergever, and Josien P.W. Pluim. Elastix: A toolbox for intensity-based medical image registration. *IEEE Trans. Med. Imaging*, 29(1):196–205, 2010. [8](#)
- [23] Weijian Li, Yuhang Lu, Kang Zheng, Haofu Liao, Chihung Lin, Jiebo Luo, Chi-Tung Cheng, Jing Xiao, Le Lu, Chang-Fu Kuo, and Shun Miao. Structured Landmark Detection via Topology-Adapting Deep Graph Learning. In *ECCV*, 2020. [1, 2, 3, 5, 8, 15](#)
- [24] Tsung Yi Lin, Piotr Dollár, Ross Girshick, Kaiming He, Bharath Hariharan, and Serge Belongie. Feature pyramid networks for object detection. In *Proc. IEEE Conf. Comput. Vis. Pattern Recognit.*, 2017. [3](#)
- [25] Ce Liu, Jenny Yuen, and Antonio Torralba. Sift flow: Dense correspondence across scenes and its applications. *PAMI*, 33(5):15–49, 2015. [3](#)
- [26] Fengze Liu, Jingzheng Cai, Yuankai Huo, Chi-Tung Cheng, Ashwin Raju, Dakai Jin, Jing Xiao, Alan Yuille, Le Lu,

Chienhung Liao, and Adam P Harrison. JSSR: A Joint Synthesis, Segmentation, and Registration System for 3D Multi-Modal Image Alignment of Large-scale Pathological CT Scans. In *ECCV*, 2020. 8

[27] Liyuan Liu, Haoming Jiang, Pengcheng He, Weizhu Chen, Xiaodong Liu, Jianfeng Gao, and Jiawei Han. On the variance of the adaptive learning rate and beyond. *arXiv preprint arXiv:1908.03265*, 2019. 5

[28] Hans Meine and Alessa Hering. Efficient Prealignment of CT Scans for Registration through a Bodypart Regressor. In *MIDL*, 2019. 9

[29] Keelin Murphy, Bram Van Ginneken, Joseph M Reinhardt, Sven Kabus, Kai Ding, Xiang Deng, Kunlin Cao, Kaifang Du, Gary E Christensen, Vincent Garcia, et al. Evaluation of registration methods on thoracic ct: the empire10 challenge. *IEEE transactions on medical imaging*, 30(11):1901–1920, 2011. 8

[30] David Novotny, Samuel Albanie, Diane Larlus, and Andrea Vedaldi. Self-Supervised Learning of Geometrically Stable Features Through Probabilistic Introspection. In *CVPR*, pages 3637–3645, 2018. 2, 4

[31] Alison Q. O’Neil, Antanas Kascenas, Joseph Henry, Daniel Wyeth, Matthew Shepherd, Erin Beveridge, Lauren Clunie, Carrie Sansom, Evelina Šeduikytė, Keith Muir, and Ian Poole. Attaining human-level performance with atlas location autocontext for anatomical landmark detection in 3D CT data. In *ECCV*, volume 11131 LNCS, pages 470–484, 2018. 3

[32] Cheng Ouyang, Carlo Biffi, Chen Chen, Turkay Kart, Huaqi Qiu, and Daniel Rueckert. Self-supervision with Superpixels: Training Few-shot Medical Image Segmentation without Annotation. In *ECCV*, 2020. 2, 5

[33] Deepak Pathak, Philipp Krahenbuhl, Jeff Donahue, Trevor Darrell, and Alexei A Efros. Context Encoders: Feature Learning by Inpainting. In *CVPR*, volume 2016-Decem, pages 2536–2544, 2016. 2

[34] Fernando Pérez-García, Rachel Sparks, and Sébastien Ourselin. TorchIO: a Python library for efficient loading, preprocessing, augmentation and patch-based sampling of medical images in deep learning. Technical report, 2020. 5

[35] Pedro O Pinheiro, Amjad Almahairi, Ryan Y Benmalek, Florian Golemo, and Aaron Courville. Unsupervised Learning of Dense Visual Representations. In *NeurIPS*, 2020. 2, 7

[36] Xavier Rafael-Palou, Anton Aubanell, Ilaria Bonavita, Mario Ceresa, Gemma Piella, Vicent Ribas, and Miguel A. González Ballester. Re-Identification and growth detection of pulmonary nodules without image registration using 3D siamese neural networks. *Med. Image Anal.*, 67:101823, 2021. 2

[37] Ignacio Rocco, Relja Arandjelovic, and Josef Sivic. End-to-End Weakly-Supervised Semantic Alignment. In *CVPR*, pages 6917–6925, 2018. 3

[38] Holger R. Roth, Christopher T. Lee, Hoo-Chang Shin, Ari Seff, Lauren Kim, Jianhua Yao, Le Lu, and Ronald M. Summers. Anatomy-specific classification of medical images using deep convolutional nets. pages 2–5, 2015. 3

[39] D Rueckert, L I Sonoda, C Hayes, D L G Hill, M O Leach, and D J Hawkes. Nonrigid Registration Using Free-Form Deformations: Application to Breast MR Images. *IEEE Trans. Med. Imaging*, 18(8), 1999. 2, 3, 5, 8, 15

[40] Abhinav Shrivastava, Abhinav Gupta, and Ross Girshick. Training region-based object detectors with online hard example mining. In *CVPR*, volume 2016-Decem, pages 761–769, 2016. 4

[41] Hessam Sokoote, Bob de Vos, Floris Berendsen, Boudewijn P.F. Lelieveldt, Ivana Išgum, and Marius Staring. Nonrigid image registration using multi-scale 3D convolutional neural networks. In *MICCAI*, volume 10433 LNCS, pages 232–239, 2017. 3

[42] Ke Sun, Bin Xiao, Dong Liu, and Jingdong Wang. Deep High-Resolution Representation Learning for Human Pose Estimation. In *CVPR*, 2019. 2, 5, 8

[43] Nima Tajbakhsh, Yufei Hu, Junli Cao, Xingjian Yan, Yi Xiao, Yong Lu, Jianming Liang, Demetri Terzopoulos, and Xiaowei Ding. Surrogate supervision for medical image analysis: Effective deep learning from limited quantities of labeled data. In *ISBI*, volume 2019-April, pages 1251–1255, 2019. 2

[44] Nima Tajbakhsh, Laura Jeyaseelan, Qian Li, Jeffrey Chiang, Zhihao Wu, and Xiaowei Ding. Embracing Imperfect Datasets: A Review of Deep Learning Solutions for Medical Image Segmentation. *Medical Image Analysis*, 2020. 1

[45] Aaron Van Den Oord, Yazhe Li, and Oriol Vinyals. Representation learning with contrastive predictive coding, 2018. 3, 4

[46] Shuxin Wang, Shilei Cao, Dong Wei, Renzhen Wang, Kai Ma, Liansheng Wang, Deyu Meng, and Yefeng Zheng. LT-Net: Label Transfer by Learning Reversible Voxel-wise Correspondence for One-shot Medical Image Segmentation. In *CVPR*, 2020. 5

[47] Shuxin Wang, Shilei Cao, Dong Wei, Renzhen Wang, Kai Ma, Liansheng Wang, Deyu Meng, and Yefeng Zheng. LT-Net: Label Transfer by Learning Reversible Voxel-wise Correspondence for One-shot Medical Image Segmentation. In *CVPR*, 2020. 5, 11

[48] Yan Wang, Yuyin Zhou, Wei Shen, Seyoun Park, Elliot K Fishman, and Alan L Yuille. Abdominal multi-organ segmentation with organ-attention networks and statistical fusion. *Med. Image Anal.*, 55:88–102, 2019. 1

[49] Zhirong Wu, Yuanjun Xiong, Stella Yu, and Dahua Lin. Unsupervised Feature Learning via Non-Parametric Instance-level Discrimination. In *CVPR*, 2018. 2, 3, 4

[50] Zhoubing Xu, Christopher P Lee, Matthias P Heinrich, Marc Modat, Daniel Rueckert, Sébastien Ourselin, Richard G Abramson, and Bennett A Landman. Evaluation of six registration methods for the human abdomen on clinically acquired ct. *IEEE Transactions on Biomedical Engineering*, 63(8):1563–1572, 2016. 8

[51] Ke Yan, Le Lu, and Ronald M. Summers. Unsupervised Body Part Regression via Spatially Self-ordering Convolutional Neural Networks. In *ISBI*, 2018. 3

[52] Ke Yan, Yifan Peng, Veit Sandfort, Mohammad Bagheri, Zhiyong Lu, and Ronald M. Summers. Holistic and com-

prehensive annotation of clinically significant findings on diverse CT images: Learning from radiology reports and label ontology. In *CVPR*, volume 2019-June, pages 8515–8524, 2019. [2](#), [5](#), [8](#)

[53] Ke Yan, Xiaosong Wang, Le Lu, and Ronald M. Summers. DeepLesion: automated mining of large-scale lesion annotations and universal lesion detection with deep learning. *Journal of Medical Imaging*, 5(3), 2018. [2](#), [5](#)

[54] Ke Yan et al. Deep Lesion Graphs in the Wild: Relationship Learning and Organization of Significant Radiology Image Findings in a Diverse Large-scale Lesion Database. In *Proc. IEEE Conf. Comput. Vis. Pattern Recognit.*, 2018. [2](#), [5](#), [8](#), [9](#)

[55] Yefeng Zheng, David Liu, Bogdan Georgescu, Hien Nguyen, and Dorin Comaniciu. Robust landmark detection in volumetric data with efficient 3D deep learning. In *MICCAI*, number 9783319429984, pages 49–61. 2015. [1](#)

[56] Zongwei Zhou, Vatsal Sodha, Jiaxuan Pang, Michael B. Gotway, and Jianming Liang. Models Genesis. *Med. Image Anal.*, 2020. [2](#)

[57] Xinrui Zhuang, Yuexiang Li, Yifan Hu, Kai Ma, Yujiu Yang, and Yefeng Zheng. Self-supervised feature learning for 3d medical images by playing a rubik’s cube. In *MICCAI*, volume 11767 LNCS, pages 420–428, 2019. [2](#)

## 6. Supplementary Material

### 6.1. Universal Anatomical Point Matching in CT

To show that SAM can be used to detect arbitrary anatomical locations, we randomly select a point in a template CT image, and then use SAM to find its matched point in a query image from another patient. Examples are demonstrated in Fig. 8. SAM can accurately find the matched anatomical location in the query image despite significant inter-subject variability, organ deformation, and contrast changes.

### 6.2. Universal Lesion Matching in DeepLesion

More qualitative examples on universal lesion matching are illustrated in Fig. 9. SAM successfully matched a variety of lesions in different body parts on the follow-up scans.

### 6.3. Template Selection for Landmark Detection

To detect landmarks in the one-shot setting, we need to select a template image from the training set. We chose the image whose landmarks are closest to the average normalized landmarks as the template, which is similar to the atlas selection method in one-shot segmentation [47]. Suppose the 3D landmark annotations for image  $i$  is  $L_i \in \mathbb{R}^{n_l \times 3}$ , where  $n_l = 19$  is the number of landmarks. We first normalized each column of  $L_i$  to  $0 \sim 1$  to get  $\tilde{L}_i$ , then computed the average normalized coordinates across samples,  $\bar{L} = \frac{1}{n_{\text{train}}} \sum_{i=1}^{n_{\text{train}}} \tilde{L}_i$ , where  $n_{\text{train}}$  is the number of training images. Last, the template image  $\hat{i}$  was selected as  $\hat{i} = \operatorname{argmin}_{1 \leq i \leq n_{\text{train}}} \|\tilde{L}_i - \bar{L}\|_F^2$ , where  $\|\cdot\|_F$  is the Frobenius norm. The template images of the 2D X-ray datasets were selected using the same approach.

### 6.4. Landmark Computation and Detection on ChestCT

The ChestCT dataset contains manually annotated masks of 35 organs for each patient. We used the organ masks to compute 19 landmarks. Take “top of aortic arch” as an example, we first found the most superior axial slice that contains the mask of “aortic arch”, and then calculated its center of mass as the landmark. These 19 landmarks include trachea bifurcation, bottom of right/left internal jugular vein, bottom of ascending aorta, top of descending aorta, top/anterior of aorta arch, 3D center of aorta arch, 3D center of heart, left end of left bronchus, left/top of pulmonary artery, 3D center of pulmonary artery, top of left/right lung, 3D center of left/right thyroid, top of sternum, and top of superior vena cava vein.

The 3D landmark detection comparison between SAM and four widely-used conventional registration methods are illustrated in Fig. 10. It can be observed that conventional registration may struggle when the two images exhibit large

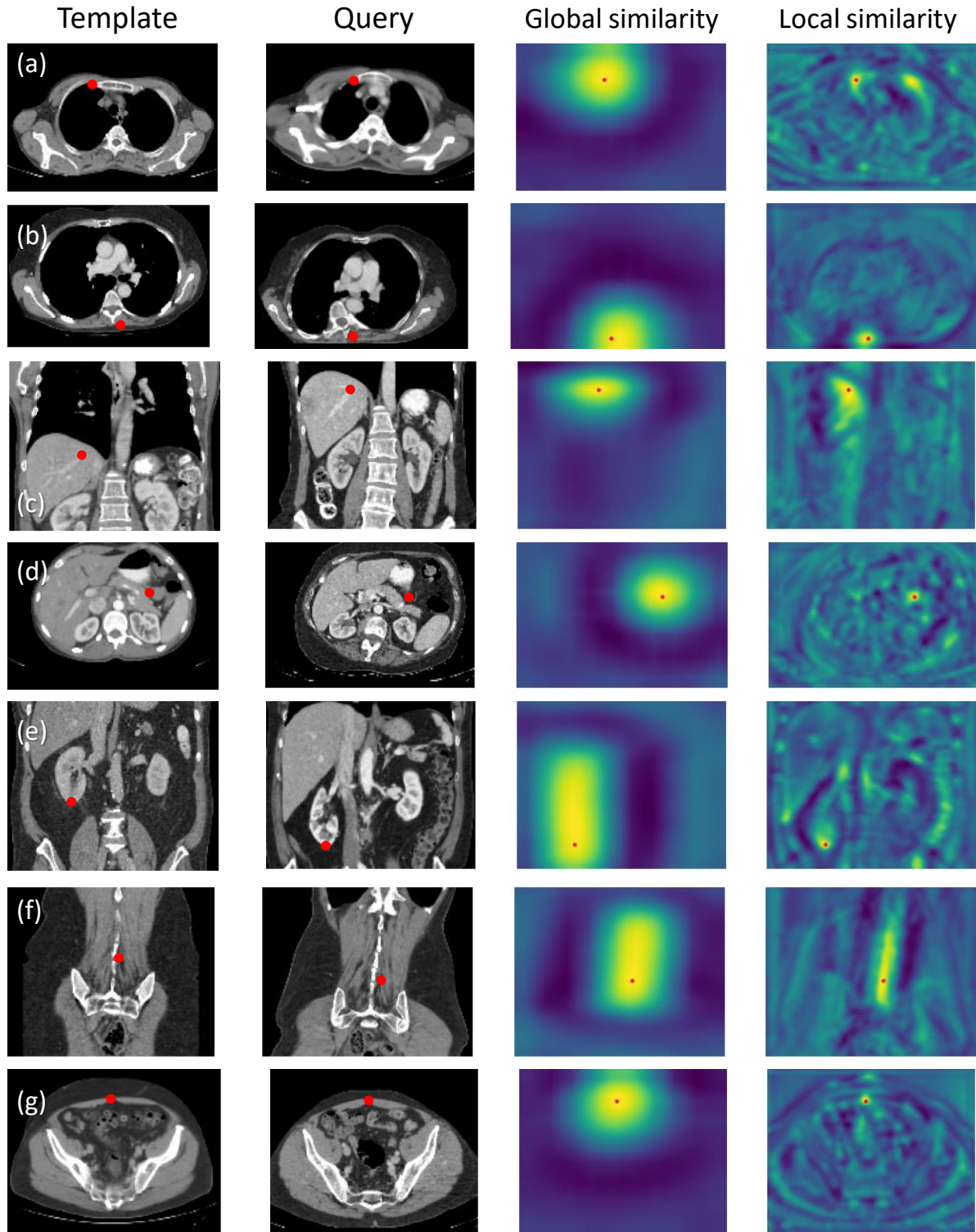


Figure 8: Random anatomical point matching results. We randomly select an anatomical point in a template CT image, and then use SAM to find its matched point in a query image from another patient. The template image, query image, global similarity map, and local similarity map are displayed in each row. The red points are selected points in template images or detected points in query images and similarity maps. The views (axial, coronal, sagittal) in each row were selected in order to clearly show the point.

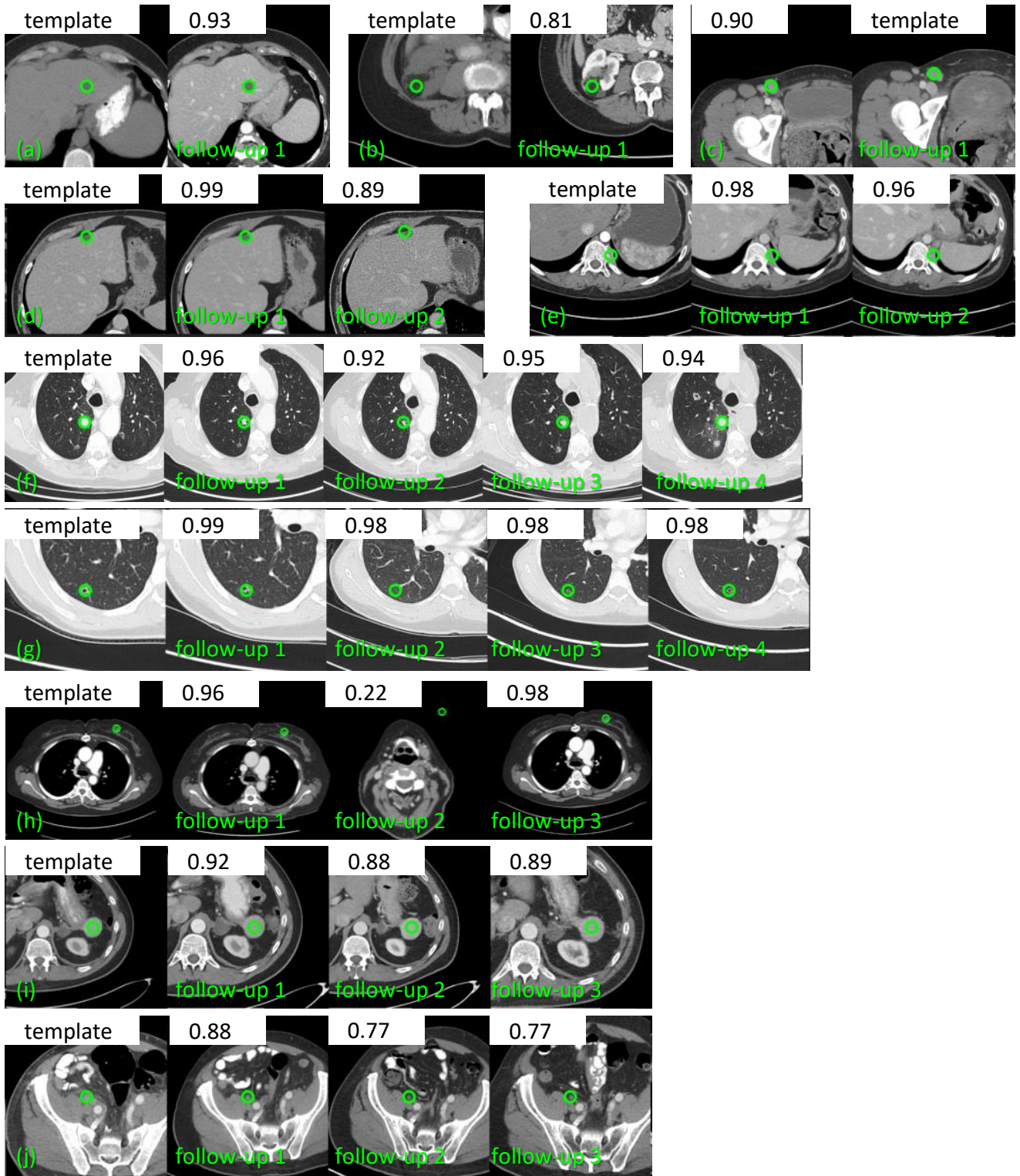


Figure 9: Examples of lesion matching results of SAM on DeepLesion. Green circles mark the lesion's central point in the template scan and the detected points in follow-up scans. The predicted similarity scores are also shown. Group (c) shows an example of using a lesion annotation from a follow-up scan as template to match lesions in earlier scans. It can help radiologists to check if the lesion has been missed in the earlier scan. Follow-up 2 of (h) is from a CT volume that does not include the chest region, so SAM matched an unrelated point with a low score.

differences in terms of body size/pose, organ shape and respiratory status, while SAM detected the landmarks more accurately with self-supervised appearance embeddings.

### 6.5. Detailed Network Architecture of SAM

The detailed 3D and 2D network architectures are illustrated in Fig. 11.

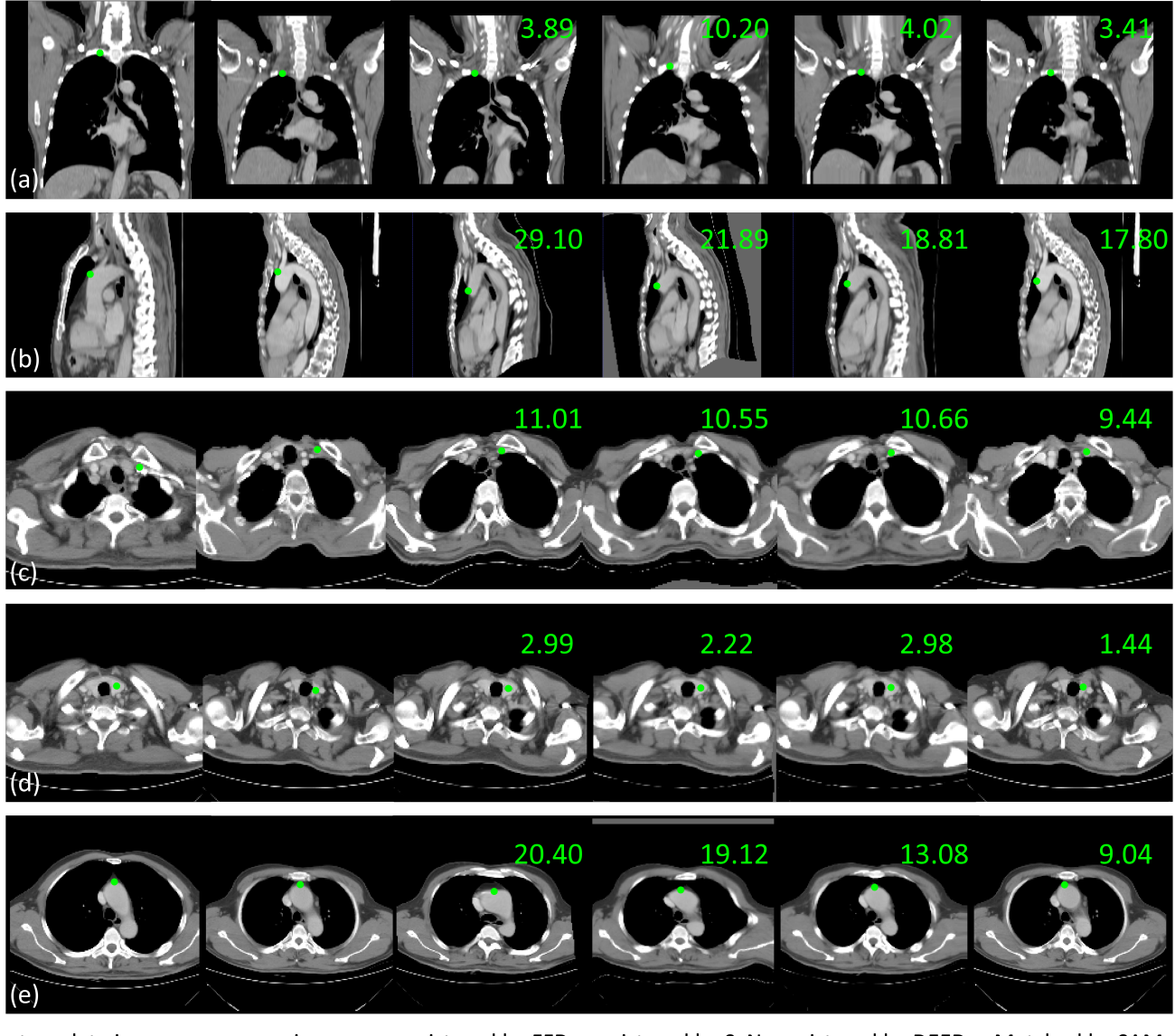


Figure 10: 3D landmark detection results in chestCT using different methods. The mean radial error [23] of each method is also shown. Columns 3 to 5 present registered/deformed template images according to the query one using FFD [39], SyN [2], and DEEDs [19], respectively. **Larger appearance inconsistency between the registered image and the query one typically indicates larger landmark detection errors.** (a) shows an example for detecting the top of right lung, where lungs in the template image are larger than those in the query one. Although most methods performed well to detect the lung top, registration based methods present obvious deformation errors near the lung bottom, especially for FFD and SyN. (b) and (c) show examples of detecting the anterior of aorta arch and bottom of internal jugular vein. The query images are quite different from the template in body pose (b) and shape (c), and registration methods exhibit large deformation error near aorta arc (b) and anterior of chest wall (c). (d) presents a case that the template and query images have different thyroid sizes, where SAM is able to provide more accurate localization. (e) shows an example where the registration methods could not perform well due to the large difference between the template image and the query one, while SAM directly matched the landmark with higher accuracy.

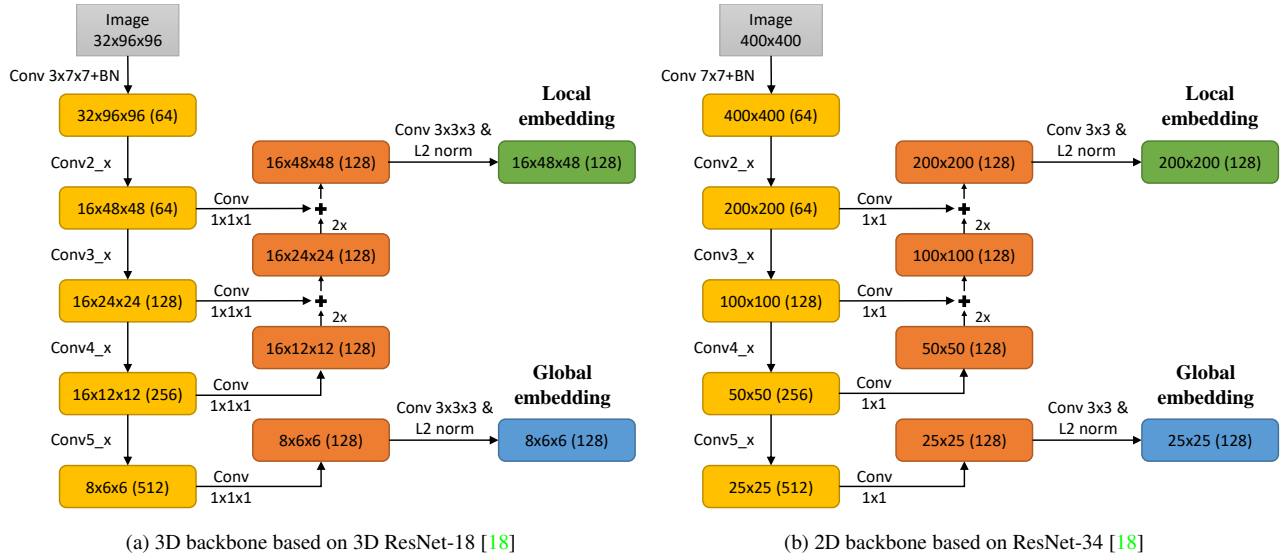


Figure 11: Coarse-to-fine network architectures for 3D and 2D images. The shapes of images and feature maps in training are shown in the format of  $z \times y \times x$  (*channel*).